Dalton Transactions

ROYAL SOCIETY OF CHEMISTRY

PAPER

View Article Online
View Journal | View Issue

Check for updates

Cite this: *Dalton Trans.*, 2022, **51**, 3146

Highly luminescent mixed-ligand bimetallic lanthanoid(III) complexes for photovoltaic applications†

Gabriela Brito-Santos, [a] Cecilio Hernández-Rodríguez, [b,c] Beatriz Gil-Hernández, [a,c] Benjamín González-Díaz, [d] Inocencio R. Martín, [b,c] Ricardo Guerrero-Lemus [b,c] and Joaquín Sanchiz *[a,c]

Received 17th December 2021,
Accepted 27th January 2022

DOI: 10.1039/d1dt04248c

rsc.li/dalton

Six new mixed-ligand bimetallic complexes $[Eu_2(bz)_4(tta)_2(phen)_2]$ (**1**), $[Gd_2(bz)_4(tta)_2(phen)_2]$ (**2**), $[EuTb(bz)_4(tta)_2(phen)_2]$ (**3**), $[EuGd(bz)_4(tta)_2(phen)_2]$ (**4**), $[Eu_{1,2}Gd_{0,8}(bz)_4(tta)_2(phen)_2]$ (**5**) and $[Eu_{1,6}Gd_{0,4}(bz)_4(tta)_2(phen)_2]$ (**6**) have been prepared with the Eu^{3+}, Gd^{3+} and Tb^{3+} ions and the benzoate (bz^-), 2-thenoyltrifluoroacetonate (tta^-) and the 1,10-phenanthroline (phen) ligands. The compounds combine highly efficient antennas to obtain highly luminescent complexes to enhance solar cell efficiency. The benzoate ligand has been chosen to take its advantage as a bridging ligand to end up with bimetallic complexes to study the effect of combining two metal ions in the luminescent molecule. The structure of **1** was obtained by single-crystal X-ray diffraction, and **1–6** were found to be isostructural by powder X-ray diffraction analysis. The photophysical properties were studied by the absorbance and emission spectra and emission lifetimes. The magnetic properties of **2** were studied, and we found intramolecular antiferromagnetic interactions between the Gd^{3+} ions. We prepared luminescent down-shifting layers (LDSL) with the **1**, **3–6** complexes embedded in ethylene–vinyl–acetate and studied their effect in the external quantum efficiency (EQE) and intensity–voltage (*I*–*V*) plots of a solar mini-module. We found that LDSL containing the bimetallic complexes **3** and **6** enhance the efficiency of the solar mini-module from 11.26(3)% to 11.76(4)% (+0.52%) and to 11.44(2)% (+0.21%), respectively.

Introduction

Photoluminescence (PL) is one of the most characteristic properties of lanthanoid^{3+} ions. This phenomenon is particularly intense for Eu^{3+} and Tb^{3+} and leads compounds containing those ions to have multiple applications in fields such as LEDs, photovoltaics, temperature and UV sensing or bioimaging, to name a few.[1–15] Although the photoluminescence process can be efficient, lanthanoid^{3+} ions themselves feature low absorption rates, limiting the emission intensity. However, the preparation of suitable lanthanoid ion complexes considerably enhances the photoluminescence intensity by the so-called antenna effect produced by organic sensitizers.[16,17] It is commonly accepted that the sensitised luminescence process starts with the excitation of the organic ligand from the singlet ground state to an excited singlet state ($S_0 \rightarrow S_n^*$). At this point, the ligand can participate in inter-system crossing to a lower energy triplet state (ISC). Next, the energy is transferred to an emissive state of the lanthanoid^{3+} ion, and finally, the lanthanoid^{3+} centred emission occurs.[18–20] The global process is called down-shifting (DS) as it results in an increase in the wavelength of the emitted radiation compared to that absorbed. This phenomenon is of particular interest for photovoltaics (PV) since it simultaneously allows the conversion of inefficient UV photons into more efficient visible ones and protects the photovoltaic device from the UV radiation responsible for the ageing of the photovoltaic modules.[2,10,21,22] For these applications, the higher the quantum yield of the overall process, the greater the interest of the compound. The best way to incorporate these compounds in the PV technology consists of their inclusion in the ethylene–vinyl acetate (EVA) or polymethylmethacrylate (PMMA) films that cover the solar modules. For such a purpose, the compounds need to be miscible and processable with those polymers.

[a]*Departamento de Química, Facultad de Ciencias, Universidad de La Laguna, Tenerife, 38206, Spain. E-mail: jsanchiz@ull.edu.es*
[b]*Departamento de Física, Facultad de Ciencias, Universidad de La Laguna, Tenerife, 38206, Spain*
[c]*Instituto Universitario de Materiales y Nanotecnología, Universidad de La Laguna, Tenerife, 38206, Spain*
[d]*Departamento de Ingeniería Industrial, Escuela Superior de Ingeniería y Tecnología, Universidad de La Laguna, Tenerife, 38206, Spain*

†Electronic supplementary information (ESI) available: PXRD patterns, additional figures and tables. CCDC 2110403 for complex **1**. For ESI and crystallographic data in CIF or other electronic format see DOI: 10.1039/d1dt04248c

The final intensity of the emission depends on the efficiency of the different stages: absorption, intersystem crossing (ISC), energy transfer (ET), and radiative deactivation of the lanthanoid ion.[16,23–25] Therefore, to have an intense luminescence, we have to prepare complexes with ligands capable of absorbing a wide range of UV wavelengths, favouring the transition to the paramagnetic triplet state of the ligands, enhancing the radiative deactivation respect to the non-radiative processes. For such a purpose, we have prepared new Eu^{3+}, Gd^{3+} and Tb^{3+} bimetallic complexes, which contain three different organic ligands (benzoate, bz^-; phenanthroline, phen; and 2-thenoyltrifluoroacetonate, tta^-), which have never been combined simultaneously but which are known to work efficiently as antennas for Eu^{3+}.[17,26–28] The combination of these three ligands gives a broad absorbance from wavelengths ranging from 220 nm to almost 400 nm. Additionally, the characteristics of the chosen ligands minimise the entry of water molecules in the metal ions' coordination sphere and enhance the processability of the material in PMMA or EVA films, which is of particular interest for photovoltaic modules.[14,29,30] We have also taken advantage of the benzoate ligand to work as a bridging ligand, which allowed us to prepare bimetallic complexes,[2,31] which in some cases have shown more intense luminescent signal than the corresponding mononuclear analogues.[32,33] Also, the benzoate ligand has a high energy triplet state that leads to the population of excited states of Tb^{3+} that tta^- could not populate.[31,34] Due to the similar sizes of the lanthanoid ions, isostructural complexes for Eu^{3+}, Gd^{3+} and Tb^{3+} are frequently obtained under otherwise the same reaction conditions, which facilitates the synthesis of hetero-bimetallic complexes.[35,36]

One of the interests of hetero-bimetallic complexes lies in the possibility of combining in the same compound the highly emissive Eu^{3+} ion with highly paramagnetic ions, such as Gd^{3+} or Tb^{3+}, which favour the intersystem crossing and reduces the concentration quenching resulting in enhanced luminescent species. It has been reported that the paramagnetic character of the Gd^{3+} and Tb^{3+} ions favour the transition from the singlet states of the ligands to their triplet states, minimising ligand fluorescence or vibrational deactivation.[16,18] Another exciting aspect of the bimetallic complexes resides in the potential intermetallic energy transfer and potential tuneable emission which may have applications in the field of LEDs, optical sensors, temperature sensing, and bioimaging.[8,31,36–40]

Thus, as a continuation of our work searching for efficient down-shifters for photovoltaic applications, in this work, we study the synthesis, the structure, the photoluminescence of six new compounds with the general formula [M1M2$(bz)_4(phen)_2(tta)_2$] where M1 and M2 can be Eu^{3+}, Gd^{3+}, Tb^{3+} and we study the effect of M1 and M2 on the photoluminescence. Moreover, we have encapsulated a photovoltaic mini-module with the compounds dispersed in an EVA film and studied the increase in the external quantum efficiency (EQE) and the evolution of the intensity–voltage (*I–V*) curves to quantify the improvement of the energy conversion in the photovoltaic process.

Experimental

Materials

All chemicals and reagents, specifically ethanol, dichloromethane, triethylamine (98%), benzoic acid (Hbz, 99.5%), 2-thenoyltrifluoroacetone (Htta, 99%), 1,10-phenanthroline (phen, 99%), UV transparent ethylene–vinyl–acetate (EVA), $Eu(NO_3)_3{\cdot}5H_2O$ (99.99%), $Gd(NO_3)_3{\cdot}6H_2O$ (99.99%), and $Tb(NO_3)_3{\cdot}5H_2O$ (99.99%), were commercially available and used without further purification unless otherwise stated. All the synthetic procedures were performed under a dinitrogen atmosphere (Scheme 1).

General methods

Elemental analyses (C, H, N, S) and FT-IR (as KBr disks, between 400 cm^{-1} and 4000 cm^{-1}) were recorded on a FLASH EA 1112 CHNS-O microanalyser and a Thermo NicolletAvatar 360 FT-IR spectrometer, respectively. UV-visible spectra between 220 nm and 800 nm were recorded on a Varian Cary 50 bio UV-Visible Spectrophotometer with samples dissolved in ethanol. Magnetic susceptibility measurements on polycrystalline samples were performed on a Quantum Design MPMS5XL SQUID magnetometer. X-ray powder diffraction patterns were recorded on a PANanalytical X'pert X-ray diffractometer with Cu Kα radiation, 1.54184 Å, at room temperature.

Synthesis of the complexes

$[Eu_2(bz)_4(tta)_2(phen)_2]$ (1) and $[Gd_2(bz)_4(tta)_2(phen)_2]$ (2). Hbz (30.5 mg, 0.250 mmol), Htta (112.8 mg, 0.508 mmol), and triethylamine (150 μl, 0.75 mmol) were added to a round-bottom flask with 9 mL of ethanol and stirred until dissolved at room temperature. Then 0.250 mmol of phen (49.6 mg) dissolved in 3 mL of ethanol were added. Finally, 0.250 mmol of the corresponding Ln^{3+} nitrate, $Eu(NO_3)_3{\cdot}5H_2O$ and $Gd(NO_3)_3{\cdot}6H_2O$ for **1** and **2** respectively, in 3 mL of ethanol, were added. The solution was heated under stirring at 60 °C under a dinitrogen atmosphere. A white precipitate appeared after 20 minutes. After 180 min the solution was cooled to room temperature, and the product was collected by filtration, washed with 5 mL of ice-cooled acetone, and air-dried at 60 °C overnight. Crystals suitable for single-crystal X-ray diffraction of **1** were obtained by slow diffusion of *n*-hexane vapour into a solution containing 10 mg of the crude product in THF. As obtained crystals of **1** and **2** were suitable for PXRD. $[Eu_2(bz)_4(tta)_2(phen)_2]$ (**1**). Yield 65.3 mg (66%). Elemental analysis (%) calcd for $C_{68}H_{44}N_4Eu_2O_{12}F_6S_2$ (1591.19): C, 51.33; H,

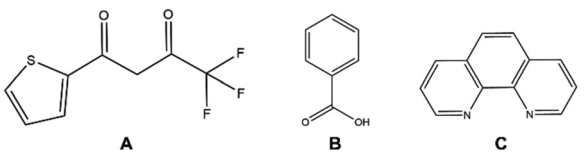

Scheme 1 Schematic drawing of 2-thenoyltrifluoroacetone (Htta), A; benzoic acid (Hbz), B; and 1,10-phenanthroline (phen), C.

2.79; N, 3.52; S, 4.03. Found: C, 50.22; H, 2.52; N, 3.37; S, 5.20. IR (KBr, n/cm^{-1}): 3065(m), 3024(m), 2926(m), 1603(s), 1572(s), 1533(m), 1410(s), 1308(s), 1182(s), 1138(s), 1061(w), 837(m), 783(m), 717(s). UV-vis (ethanol, l_{max}/nm): 227, 230, 267, 271, 292, 346.

$[Gd_2(bz)_4(tta)_2(phen)_2]$ (**2**). Yield 53.9 mg (54%). Elemental analysis (%) calcd for $C_{68}H_{44}N_4Gd_2O_{12}F_6S_2$ (1601.76): C, 50.99; H, 2.77; N, 3.50; S, 4.00. Found: C, 49.13; H, 2.42; N, 3.57; S, 5.31. IR (KBr, n/cm^{-1}): 3065(m), 3024(m), 2926(m), 1603(s), 1572(s), 1533(m), 1410(s), 1308(s), 1182(s), 1138(s), 1061(w), 837(m), 783(m), 717(s). UV-vis (ethanol, l_{max}/nm): 227, 230, 267, 271, 292, 346.

$[EuTb(bz)_4(tta)_2(phen)_2]$ (3), $[EuGd(bz)_4(tta)_2(phen)_2]$ (4), $[Eu_{1,2}Gd_{0,8}(bz)_4(tta)_2(phen)_2]$ (5) and $[Eu_{1,6}Gd_{0,4}(bz)_4(tta)_2(phen)_2]$ (6). These compounds were prepared following the previous procedure, just changing the amounts of the corresponding Ln^{3+} nitrates which are given in Table S1.† The different lanthanoid^{3+} nitrates were dissolved together and added to the reaction flask. Recrystallization of **3–6** by liquid–vapour diffusion with chloroform/*n*-hexane resulted in crystals suitable for PXRD and PV measurements. $[EuTb(bz)_4(tta)_2(phen)_2]$ (**3**). Yield 43.8 mg (44%). Elemental analysis (%) calcd for $C_{68}H_{44}N_4EuTbO_{12}F_6S_2$ (1598.15): C, 51.10; H, 2.77; N, 3.51; S, 4.01. Found: C, 51.37; H, 2.58; N, 3.71; S, 4.32. IR (KBr, n/cm^{-1}): 3065(m), 3024(m), 2926(m), 1603(s), 1572(s), 1533(m), 1410(s), 1308(s), 1182(s), 1138(s), 1061(w), 837(m), 783(m), 717(s). UV-vis (ethanol, l_{max}/nm): 227, 230, 267, 271, 292, 346. $[EuGd(bz)_4(tta)_2(phen)_2]$ (**4**). Yield 51.9 mg (52%). Elemental analysis (%) calcd for $C_{68}H_{44}N_4EuGdO_{12}F_6S_2$ (1596.47): C, 51.16; H, 2.78; N, 3.51; S, 4.02. Found: C, 50.00; H, 2.44; N, 3.55; S, 4.98. IR (KBr, n/cm^{-1}): 3065(m), 3024(m), 2926(m), 1603(s), 1572(s), 1533(m), 1410(s), 1308(s), 1182(s), 1138(s), 1061(w), 837(m), 783(m), 717(s). UV-vis (ethanol, l_{max}/nm): 227, 230, 267, 271, 292, 346. $[Eu_{1,2}Gd_{0,8}(bz)_4(tta)_2(phen)_2]$ (**5**). Yield 33.3 mg (34%). Elemental analysis (%) calcd for $C_{68}H_{44}N_4Eu_{1,2}Gd_{0,8}O_{12}F_6S_2$ (1595.42): C, 51.19; H, 2.78; N, 3.51; S, 4.02. Found: C, 51.15; H, 2.70; N, 3.57; S, 4.09. IR (KBr, n/cm^{-1}): 3065(m), 3024(m), 2926(m), 1603(s), 1572(s), 1533(m), 1410(s), 1308(s), 1182(s), 1138(s), 1061(w), 837(m), 783(m), 717(s). UV-vis (ethanol, l_{max}/nm): 227, 230, 267, 271, 292, 346. $[Eu_{1,6}Gd_{0,4}(bz)_4(tta)_2(phen)_2]$ (**6**). Yield 49.0 mg (50%). Elemental analysis (%) calcd for $C_{68}H_{44}N_4Eu_{1,6}Gd_{0,4}O_{12}F_6S_2$ (1593.30): C, 51.26; H, 2.78; N, 3.52; S, 4.02. Found: C, 51.15; H, 2.61; N, 3.48; S, 4.28. IR (KBr, n/cm^{-1}): 3065(m), 3024(m), 2926(m), 1603(s), 1572(s), 1533(m), 1410(s), 1308(s), 1182(s), 1138(s), 1061(w), 837(m), 783(m), 717(s). UV-vis (ethanol, l_{max}/nm): 227, 230, 267, 271, 292, 346.

Single-crystal X-ray structure determination

Data collection. Single-crystal XRD data for **1** were collected with an Agilent SuperNova diffractometer with a micro-focus X-ray under Cu-K_α radiation (λ = 1.5418 Å). CrysalisPro software was used to collect, index, scale and apply analytical absorption correction based on the multiscan method.[41]

Structure analysis and refinement. The structure was solved by direct methods with SHELXL2016.[42] Full-matrix least-squares refinement on F^2 with the SHELXL-2016 program suite and the ShelXle graphical user interface (GUI) was performed.[43] Crystal data and details of the structure refinement are given in Table 1. The graphics and the simulated PXRD patterns were obtained with Diamond.[44]

All non-hydrogen atoms in the structure were refined with anisotropic thermal parameters.

The hydrogen atom in α position of 2-thenoyltrifluoroacetonate, H3B, was found in the differences map and it was refined using a DFIX restraint for its C–H distance. Aromatic hydrogen atoms were all positioned geometrically (C–H = 0.93 Å) and refined using a rigid model (AFIX 43) with $U_{iso}(H) = 1.2U_{eq}(C)$.

Since the thermal anisotropic displacement parameters indicated prolate ellipsoids, all non-hydrogen atoms of the thiophene ring and benzoate group labelled C were refined with RIGU and SIMU restraints; leading the thermal parameters to behave more properly. In addition, the thiophene ring displays typical substitutional disorder for this group of adjacent sulphur and carbon atoms. This substitutional disorder was modelled with PART commands and DFIX restraints.

Photoluminescence measurements

All the measurements were performed on polycrystalline solid-state samples. Emission measurements were recorded on a Photoluminescence Spectrometer FLS 1000. The samples were excited with a 450 W Xe arc lamp with λ_{exc} = 350 nm. The lifetimes were measured with a LeCroy WS 424 Oscilloscope, where an EKSPLA/NT342/3/UVE Optical Parametric Oscillator (OPO) laser was used to excite the sample. The absolute fluorescence quantum yields (PLQY) were calculated using the 'Indirect Method' with an FLS1000 fluorimeter (Edinburgh

Table 1 Crystal data and structure refinement for $[Eu_2(bz)_4(tta)_2(phen)_2]$

Empirical formula	$C_{68}H_{44}Eu_2F_6N_4O_{12}S_2$
M/g mol^{-1}	1591.11
Temperature (K)	293
λ/Å	1.54184
Crystal system, space group	Triclinic, $P\bar{1}$
a, b, c(Å)	10.4570(4), 12.0687(6), 14.0081(7)
α, β, γ (°)	94.967(4), 103.974(4), 111.457(4)
V (Å^3)	1566.40(13)
Z	1
D_{calc}/g cm^{-3}	1.687
μ/(mm^{-1})	15.539
Theta range	4.012–72.648
No. of measured, independent and observed [$I > 2\sigma(I)$] reflections	11 462, 6027, 5440
R_{int}	0.057
R_1 [$I > 2\sigma(I)$][a]	0.0487
wR_2 [$I > 2\sigma(I)$][b]	0.1072
GOF on F^2 [b]	1.003

[a] $R_1 = [\sum(||F_o| - |F_c||)/\sum|F_o|]$. [b] $wR_2 = [\sum[w(F_o^2 - F_c^2)^2]/\sum[w(F_o^2)^2]]^{1/2}$ goodness-of-fit $S = [\sum[w(F_o^2 - F_c^2)^2]/(n-p)]^{1/2}$.

company) and an integration sphere. In this method, the quantum yield is calculated with eqn (1).

$$\mathrm{PLQY} = \frac{S_A(E_C - E_A) - S_C(E_B - E_A)}{S_A(S_B - S_C)} \quad (1)$$

where S and E correspond to the integrals of the excitation peak and emission of the sample, respectively, the subscripts A, B, and C refer to the measurement of direct excitation of the blank, direct and indirect excitation of the sample. The equipment was calibrated with [Eu(phen)(tta)$_3$] with a quantum yield of 69%.[45]

Preparation of the films on a 25 × 20 × 1 mm glass. 350 μL of CH_2Cl_2 with 10 mg of complex (**1**, **3–6**), mixed with 25 mg of EVA in 1.5 mL of CH_2Cl_2 were deposited dropwise on a bare glass (25 × 20 × 1 mm) previously washed with a 2 M sulfuric acid solution, rinsed with deionised water, and dried with dinitrogen. Then the solvent was evaporated at room temperature to obtain a thin film which was consequently encapsulated on a PV mini-module for the EQE and current/voltage (*I–V*) curves studies. The films absorb most UV radiation, but the transmittance is high in the visible region (Fig. S1†).

Encapsulation of the films on the PV mini-module. The samples were encapsulated by a standard procedure.[46] After the interconnection and the metallic contact welding, the solar cell was covered with the previously described glasses, containing the down-shifter dispersed in EVA. Then they are encapsulated on the mc-Si PV mini-module as shown in Scheme 2. The encapsulated cell was obtained after curing at 150° C under vacuum.[47] A Tedlar–polyester–Tedlar layer was used as a back sheet to protect the whole structure against climatic conditions.[48,49] An estimated reduction of 2.25% in short-circuit current density can be deduced when a new glass is used with an EVA film on top of the mini-module. In some experiments, a hemispheric aluminium reflector was placed above the film to redirect most of the downshifted photons to the solar cell, as previously described.[3]

EQE and *I–V* measurements of the PV mini-module covered with the Luminescent down-shifting films

For the EQE measurements, UV to IR optical radiation was recorded with the Oriel Merlin Digital Lock-in radiometry system (control unit, preamplifier, and optical chopper 8–1100 Hz) with a sensitivity of 0.5 μV. The typical values measured are in the range of 10 mV. Dual Xenon & Quartz Halogen Source (250–2500 nm) housing a 75 W short-arc xenon lamp and a 100 W quartz halogen lamp with automated selection through an Oriel Cornerstone 260 motorised high resolution 1/4 m monochromator, scanning from 280 nm to 2200 nm was used. The Optical system includes TracQ-Basic software. We have followed the reference cell method[50] and the standard recommendations of previous works.[3,51] A standard crystalline silicon cell from Rera Solutions BV was used as a reference, from which we have determined the input power. The external quantum efficiency (EQE) was calculated following eqn (2), where I_{sc} is the short circuit current, P_L is the power of the incident light, λ is the wavelength, e is the elementary charge, h is the Planck's constant, and c is the speed of light.[42]

$$\mathrm{EQE} = \frac{I_{sc}/e}{P_L/\left(h\frac{c}{\lambda}\right)} \quad (2)$$

The mini-module employed for the EQE and *I–V* measurements was fabricated and encapsulated with EVA in the Fraunhofer ISE. It exhibits an efficiency of 11.26(3)%.

I–V curves were measured with a Keithley 2400 Source Meter and an Abet Technologies Solar Simulator that produces one sun output. This station includes *I–V* measurement software with an interface compatible with Windows 10. The software displays the raw *I–V* curve and calculates the critical cell performance parameters such as the short circuit current density (J_{sc}) and the efficiency (η) with a current measurement sensitivity and efficiency measurement resolution of 0.05 μA and 0.02%, respectively.

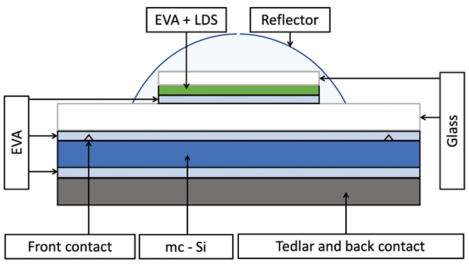

Scheme 2 Schematic drawing of photovoltaic mini-module (cross-section) and a luminescent down-shifting (LDS) layer encapsulated onto the surface of the mini-module. The down-shifting layer absorbs short wavelength photons and then re-emits them at a longer wavelength where the mc-Si solar cell exhibits a better EQE or spectral response.

Results and discussion

Synthesis and X-ray powder pattern diffractograms

The synthesis and characterization of [Eu$_2$(bz)$_4$(tta)$_2$(phen)$_2$] (**1**), [Gd$_2$(bz)$_4$(tta)$_2$(phen)$_2$] (**2**), [EuTb(bz)$_4$(tta)$_2$(phen)$_2$] (**3**), [EuGd(bz)$_4$(tta)$_2$(phen)$_2$] (**4**), [Eu$_{1,2}$Gd$_{0,8}$(bz)$_4$(tta)$_2$(phen)$_2$] (**5**) and [Eu$_{1,6}$Gd$_{0,4}$(bz)$_4$(tta)$_2$(phen)$_2$] (**6**) is a continuation of our studies in the photovoltaics (PV) applications of [Eu$_2$(bz)$_6$(phen)$_2$] and [Eu(tta)$_3$(phen)].[2,3,22,52–54] The excellent luminescent properties of the latter are known for more than 50 years,[28] and the former is dinuclear and also very luminescent with the benzoate acting as terminal and bridging ligand. Despite the high luminescence of [Eu$_2$(phen)$_2$(bz)$_6$], its absorbance is very low above 300 nm and, therefore, with limited applications as a down-shifter in PV. On the other hand, the tta$^-$ ligand has a high absorbance around 350 nm, which makes [Eu(phen)(tta)$_3$] very active in a spectral region more significant in solar radiation. So, we came up with the idea of preparing a compound that would combine a significant absorbance in the near-UV (we need tta$^-$) with a bimetallic character (we need bz$^-$) to explore the effect in the PV applications of including more than one metal ion in a highly luminescent molecule.

With that idea in mind, we tried to obtain $[Eu_2(bz)_4(tta)_2(phen)_2]$ (**1**) with the ratio of reagents corresponding to its stoichiometry. However, we obtained a compound with an elemental analysis corresponding to the formula $[Eu_2(bz)_5(tta)(phen)_2]$ but for which we were not able to obtain a single-crystal suitable for X-ray diffraction. However, we could confirm that its powder diffractogram did not correspond to $[Eu(bz)_6(phen)_2]$ nor $[Eu(tta)_3(phen)]$ and over time, we were able to verify that it did not correspond to **1**. Nevertheless, following these other reagent ratios

$$4Eu(NO_3)_3 + 4phen + 8Htta + 4Hbz + 12N(CH_2CH_3)_3 \rightarrow [Eu_2(bz)_4(tta)_2(phen)_2] + 2[Eu(tta)_3(phen)] + 12HN(CH_2CH_3)_3NO_3$$

A crude product containing a mixture of **1** and $[Eu(tta)_3(phen)]$ was obtained; both were identified by X-ray powder diffraction patterns (Fig. S2†). $[Eu(tta)_3(phen)]$ was removed washing with acetone, and we ended up with **1** in high purity, as can be seen in elemental analysis and powder diffractograms, but at the cost of lowering the yield. Following this procedure, with the appropriate ratio of the corresponding Ln^{3+} nitrates (Table S1†), compounds **2–6** were isolated. However, the isostructural Tb_2 compound was not obtained. Instead, we obtained an unknown crystalline material whose powder diffractogram did not match that of **1** (Fig. S3†). Compounds **1–6** crystallise with a 9-coordination for the lanthanoid ion. We think that the preference of the Tb(III) ion for a coordination number of 8 results in a different structure.[55] We will study the properties of this compound as soon as we have its crystal structure.

We obtained single-crystal suitable for X-ray diffraction of **1** by dissolving the product in THF and precipitating it with hexane vapour in a closed flask. This procedure led to a polycrystalline material suitable for powder X-ray diffraction and other measurements for **2–6**. By positive matching of the experimental powder diffractograms with that simulated from the single crystal of **1**, we could conclude that the single crystal of **1** corresponded to the bulk material of **1** and that all the compounds were isostructural (Fig. S3†).

The compounds $[Eu_{1,2}Gd_{0,8}(bz)_4(tta)_2(phen)_2]$ (**5**) and $[Eu_{1,6}Gd_{0,4}(bz)_4(tta)_2(phen)_2]$ (**6**) have fractional numbers for Eu^{3+} and Gd^{3+} since they contain homogeneously distributed the two structurally equivalent molecules $[Eu_2(bz)_4(tta)_2(phen)_2]$ and $[EuGd(bz)_4(tta)_2(phen)_2]$ in a certain ratio (Table S1†). In principle, we can estimate each molecule's molar fraction with the ratio of the corresponding Ln^{3+} nitrates used in the synthesis, and with that ratio, we can calculate the coefficients for Gd and Eu. We confirmed this aspect in the magnetic study.

Crystal structure description

Compounds **1–6** are isostructural and crystallise in the triclinic $P\bar{1}$ space-group as neutral centrosymmetric dinuclear molecules of $[M_2(bz)_4(tta)_2(phen)_2]$ with two 2-thenoyltrifluoroacetonate (tta^-), two phenanthroline (phen), and four bridging benzoate (bz^-) ligands (Fig. 1a and b and Fig. S5†).

M_2 metal-ions can be Eu_2, Gd_2, EuTb or EuGd. Single-crystals suitable for X-ray diffraction were obtained for the Eu_2 compound so that we will discuss compound **1** structure, but the description is valid for the rest with no significant changes in the distances and angles.[56] The Eu^{3+} ions are in nine-coordination with a distorted capped square-antiprism environment (Fig. 1c and d). Two phenanthroline nitrogen atoms (N1A and N2A), two tta^- oxygen atoms (O1B and O2B), and five benzoate oxygen atoms (O1C, O1D, O2D, O2C, and $O1D^i$) fill the coordination sphere of the Eu^{3+} ions with no solvent molecules, [symmetry code: (i) $-x$, $-y+1$, $-z+1$]. The bond distances and angles are within the expected values and reported in Table 2 and Table S2.†[2,5,31,52,57] The Eu1–$O1D^i$ is the longest distance and this atom fills the top position of the caped square-antiprism, Fig. 1d.[58]

The tta^- and phen act as terminal ligands and appear in *trans* position to each other. The chelating mode, the distances, and the angles are typical for these ligands. The thiophene ring of the tta^- ligand shows disorder in the C6B1 and S1B1 atoms because of the C4B–C5B rotation. C–H$\cdots\pi$ intramolecular interactions take place between thiophene C–H and the phenanthroline ring with a C–H$\cdots$phenanthroline-centroid distance of 2.800(2) Å.

The carboxylate groups of the four benzoate ligands bridge the two Eu^{3+} atoms. Two of them adopt the symmetric *syn–syn* mode μ-κO:κO′ (Fig. 1a), whereas the other two appear in a chelating–bridging fashion with a μ-O:κ^2O,O′ coordination mode (Fig. 1b). The combination of these four bridges results in an $Eu^{3+}\cdots Eu^{3+}$ intramolecular distance of 4.0518(3) Å, which is shorter than that found in $[Eu_2(bphen)_2(bz)_6]$, 5.5441(1) Å, for which two benzoates act as bridging in the μ-κO:κO′ mode; but longer than that found in $[Eu_2(phen)_2(bz)_6]$, 3.9604(1) Å, with an equivalent bridging mode to that of **1**, two μ-κO:κO′ and two μ-O:κ^2O,O′ (bphen = 4,7-biphenyl-1,10-phenanthroline).[2,52] The Eu–O–Eu and the Eu–O–C angles in the μ-O:κ^2O,O′ bridges are designed as θ and φ parameters and are considered of special importance for the description of the magnetic properties (Fig. S6†). These parameters take values of 101.903(2)° and 84.881(2)° for θ and φ, respectively.[59]

Each dinuclear unit is linked to other six by intermolecular C–H$\cdots\pi$ interactions between benzoate C–H and thiophene rings and between phenanthroline C–H and thiophene rings to afford a two-dimensional supramolecular network (benzoate H$\cdots$thiophene centroid, 2.8875(1) Å; phenanthroline H$\cdots$thiophene centroid 2.9595(1) Å), (Fig. S7†). The minimum $Eu^{3+}\cdots Eu^{3+}$ intermolecular distance is 8.9743(5) Å.

Magnetic properties

The temperature dependence of the $\chi_M T$ product for compound **2** is shown in Fig. 2, where χ_M corresponds to the magnetic susceptibility per two Gd^{3+} ions. The value observed at room temperature is 15.58 emu mol^{-1} K; somewhat lower than that expected for two magnetically isolated Gd^{3+} ions [expected value 15.78 emu mol^{-1} K with $g = 2.0$ and $S = 7/2$]. On lowering T, the $\chi_M T$ product slightly increases to reach the expected

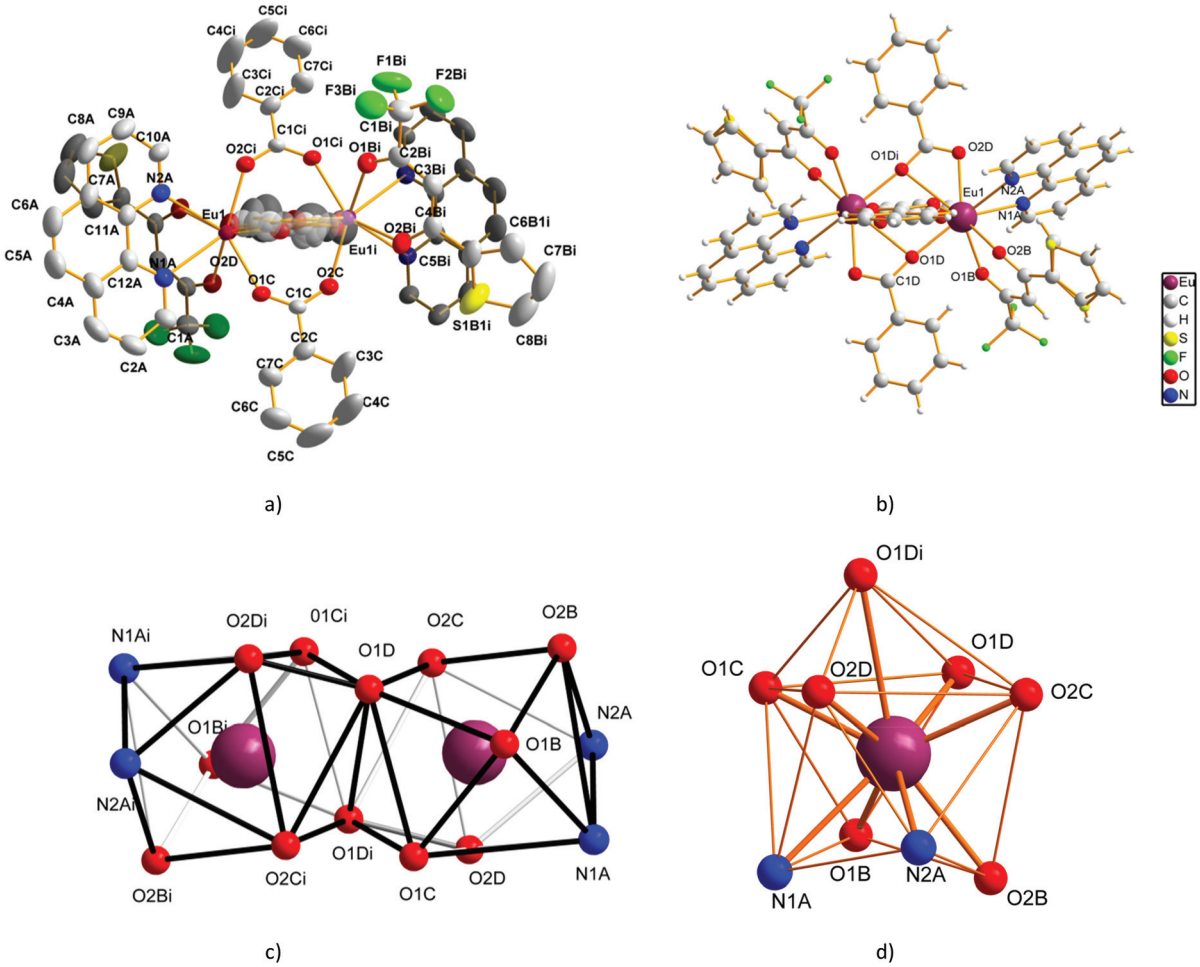

Fig. 1 (a) Structure of **1** with atoms as ellipsoids at 30% probability. Hydrogen atoms not shown. (b) A different view of **1** in ball and sticks model showing the other two bridging benzoates. (c) Coordination environment of Eu^{3+} ions in **1**. (d) Detailed view of the capped square antiprism environment of Eu^{3+} in **1**, symmetry code: (i) $-x, -y + 1, -z + 1$.

Table 2 Main distances (Å) in **1**

Eu1–O1D	2.341(3)	Eu1–O1B	2.453(3)
Eu1–O2C^{i}	2.353(3)	Eu1–N1A	2.605(4)
Eu1–O1C	2.378(3)	Eu1–N2A	2.657(4)
Eu1–O2B	2.403(3)	Eu1–O1D^{i}	2.860(4)
Eu1–O2D^{i}	2.423(3)	Eu1···Eu1^{i}	4.0518(3)

Symmetry code: (i) $-x, -y + 1, -z + 1$.

value and then remains almost constant up to 50 K. Finally continuously decreases to reach a minimum value of 13.21 emu mol^{-1} K at 2 K. This behaviour is indicative of the existence of weak intramolecular antiferromagnetic interactions between the Gd^{3+} ions in **2**. Gd^{3+} ions have an $^{8}S_{7/2}$ ground state, and therefore, they are very isotropic and significant zero-field-splitting effects are not expected or cannot be unambiguously determined in polycrystalline samples.[60,61] Also, we can discard intermolecular interactions since the interaction

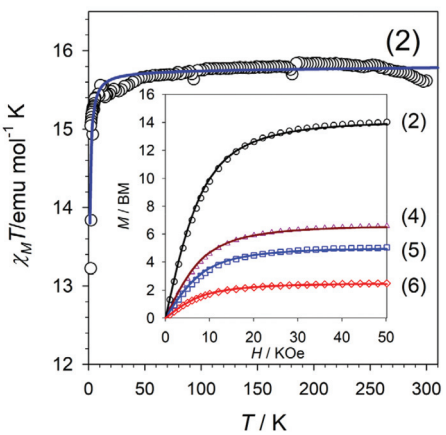

Fig. 2 Temperature dependence of the $\chi_M T$ product for compound **2**: (O), experimental; (solid line), calculated curve. The inset shows the magnetization *vs.* H plot at 2 K for **2**, **4**–**6**. The symbols correspond to the experimental data, whereas the solid lines correspond to the best fit to the magnetisation equation.

becomes noticeable just below 50 K and the $Gd^{3+}\cdots Gd^{3+}$ intermolecular distance is above 11 Å.

The intramolecular magnetic coupling occurs through the two symmetric *syn–syn* and the two oxo-carboxylate bridges; the μ-κO:κO′ and the μ-O:κ^2O,O′, respectively, Fig. 1a and b. Under that approach, the magnetic data were analysed with the corresponding equation for two interacting spin octets derived from the isotropic spin Hamiltonian $\hat{H} = -J\hat{S}_1\hat{S}_2$.[56,62] The calculated curve (Fig. 2 solid dark blue line) fitted well the data and the best-fit parameters were found to be $g = 2.00(1)$, $J = -0.021(1)$ cm^{-1} and $R = 1.14 \times 10^{-4}$. (R is defined as $\sum_i \left[(\chi_M T)_{obs}(i) - (\chi_M T)_{calc}(i)\right]^2 / \sum_i \left[(\chi_M T)_{obs}(i)\right]^2$). Gd^{3+} dinuclear compounds connected by carboxylate bridges may exhibit different bridging modes, described as A, B and C according to Baggio *et al.*[59,63] Several experimental and theoretical magneto-structural studies have been performed in this kind of compounds, but a clear correlation related to a specific parameter has not been found yet.[64] Nevertheless, the most important parameters are the intermetallic $Gd^{3+}\cdots Gd^{3+}$ distances, and the θ and φ parameters (Fig. S6†).[59,64] The value obtained for **1** falls within the range previously found in well-characterised Gd^{3+} dinuclear complexes exhibiting the same kind of bridging mode with similar structural parameters for which values ranging from −0.021 cm^{-1} to −0.043 cm^{-1} are reported.[59,65,66]

The inset of Fig. 2 shows the magnetisation plots as a function of the applied magnetic field for **2**, **4–6** at 2 K. At this temperature, the ground state of Gd^{3+} and Eu^{3+} ions are the only populated. The Gd^{3+} ground state $^8S_{7/2}$ has a spin number $S = 7/2$, whereas the Eu^{3+} $^7F_0$ is diamagnetic. Thus the fit of the data to the magnetisation equation can give us the amount of Gd^{3+} in **2**, **4–6**. The magnetization equation is given by $M = ngSB_S(y)$, where $y = g\beta SH/kT$ and $B_S(y)$ is the Brillouin function defined by

$$B_S(y) = \frac{2S+1}{2S}\coth\left(\frac{2S+1}{2S}\right) - \frac{1}{2S}\coth\left(\frac{1}{2S}y\right) \quad (3)$$

the other parameters are n, the number of Gd^{3+} ions; g, the Landé factor for Gd^{3+}; S, the spin number for Gd^{3+}; β, the Böhr magneton; H, the applied magnetic field; k, the Boltzman constant and T the temperature.[62] The calculated magnetisation curves are shown in the graphic as solid lines and reproduce very well the experimental values. The calculated n values are very close to the expected ones and are shown in Table 3. This magnetic study indicates that the formulas proposed for the compounds are correct and that the synthesis process allowed us to obtain the bimetallic compounds in the desired ratios.

Photophysical properties

Solution UV-vis spectra. The UV-vis absorption spectra of **1–6** complexes and free ligands dissolved in ethanol are represented in Fig. 3. All complexes spectra have the same pattern because the absorption is due to the $S_0 \rightarrow S_n^*$ transitions of the ligands. Complexes' absorption shows a considerable increase compared to the free ligands (line in short dash style in the figure) since the complexes contain two molecules of phenanthroline, four benzoate molecules, and two diketonate ligands per mole of complex. In addition, the increase in rigidity when forming the complexes favours the absorption of the radiation. The first absorption band at 227 nm with a shoulder at 230 nm is due to the contribution of benzoate and phenanthroline, respectively, the phenanthroline molecule causes the second band at 271 nm with a shoulder at 292 nm, and the last band at 346 nm shows bathochromic shift respect to the absorptions of the tta$^-$ ligand at 336 nm. The excited singlet-state energies of the ligands take values of 44.000 cm^{-1}, 37.000 cm^{-1}, and 28.900 cm^{-1} for benzoate, phen, and tta$^-$ respectively, corresponding with those previously reported.[67,68]

Solid-state room-temperature photoluminescence. Photoluminescence emission spectra (λ_{exc} = 350 nm) of the Eu^{3+} containing complexes (**1**, **3–6**) are shown in Fig. 4a. All the compounds exhibit intense emission with the characteristic sharp peaks in the 570–730 nm range associated with the $^5D_0 \rightarrow$

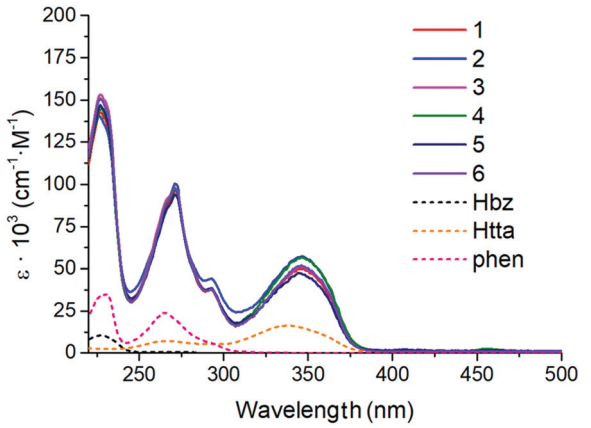

Fig. 3 UV-Vis region molar absorption (ε) of complexes **1–6** and free ligands dissolved in ethanol.

Table 3 Total content of Gd^{3+} ion per formula in compounds **2**, **4–6**

Compound	$n_{expected}$	$n_{calculated}$	R^a	Calculated formula
2	2	2	0.99	$[Gd_2(bz)_4(tta)_2(phen)_2]$
4	1	0.93	0.99	$[Eu_{1.07}Gd_{0.93}(bz)_4(tta)_2(phen)_2]$
5	0.8	0.72	0.99	$[Eu_{1.28}Gd_{0.72}(bz)_4(tta)_2(phen)_2]$
6	0.4	0.35	0.99	$[Eu_{1.65}Gd_{0.35}(bz)_4(tta)_2(phen)_2]$

[a] $R^2 = \sum_i \left(M_i^{calc} - \bar{M}\right)^2 / \sum_i (M_i - \bar{M})^2$.

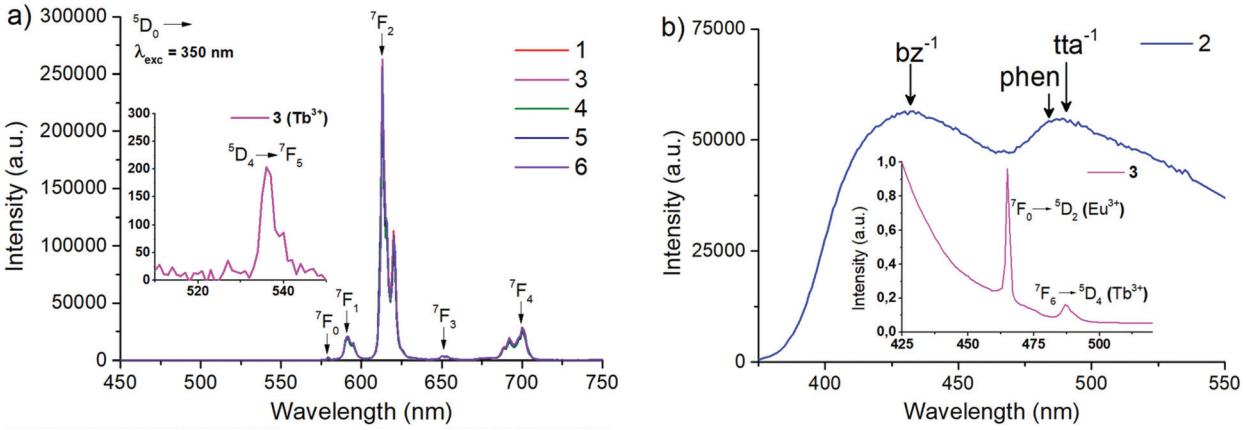

Fig. 4 (a) Room-temperature photoluminescence spectra of Eu^{3+} containing complexes, λ_{exc} = 350 nm. The inset shows the Tb^{3+} $^5D_4 \rightarrow {}^7F_5$ transition in **3**. (b) Ligand phosphorescence emission spectra in complex **2**, λ_{exc} = 350 nm. The inset shows the excitation spectrum of **3** detecting at 612 nm.

$^7F_{0-4}$ transitions of the Eu^{3+} ion resulting in the typical red colour of the Eu^{3+} complexes.

We observe two broad bands centred at 435 nm and 490 nm in the emission spectrum of compound **2**, Fig. 4b. The energy of the excited states of the Gd^{3+} ion is too high to be populated, and the emission spectrum corresponds to the decay of the triplet states of the ligands (phosphorescence). The band at 435 nm corresponds to the deactivation of the triplet state of the benzoate (23 000 cm^{-1}), the other one around 490 nm corresponds indistinguishable to the deactivation of the triplet states of phenanthroline and tta^- (20 790 cm^{-1} and 20 450 cm^{-1}, respectively).[33,69] It is noteworthy that in the emission spectra (Fig. 4a), the excitation occurs at 350 nm where only the tta^- ligand presents absorption. However, compound **2** shows phosphorescence at wavelengths which do not only correspond to the deactivation of the triplet state of tta^- (20 450 cm^{-1}). This indicates the existence of intersystem crossing (ISC) from the excited singlet states of the tta^- (28 900 cm^{-1}) not only to the triplet state of tta^- but also to those of benzoate and phenanthroline ligands. The activation of the triplet state of the benzoate enables the population of the $^5D_4$ excited state of Tb^{3+} in **3**, since the triplet state of tta^- does not have enough energy (20 450 cm^{-1}) to populate the excited states of Tb^{3+} ($^5D_4$ 20 430 cm^{-1}).[34] It has to be noted that at least 2500 cm^{-1} of difference are required for an effective ET from the triplet state of the ligand to the Tb^{3+} to avoid the back-transfer (BT).[1,20]

In order to investigate a hypothetical energy transfer from Tb^{3+} ($^5D_4$) to Eu^{3+} ($^5D_1$ or $^5D_0$), we measured the excitation spectrum of compound **3** detecting at 612 nm (inset Fig. 4b and Fig. S8†). That spectrum shows a broad band in the range of 225 nm to 450 nm corresponding to the absorption of the bz^-, phen and tta^- ligands, a peak around 465 nm corresponding to the absorption of Eu^{3+} (21 500 cm^{-1}, $^7F_0 \rightarrow {}^5D_2$) and a second transition at 490 nm corresponding to the absorption of Tb^{3+} ($^7F_6 \rightarrow {}^5D_4$, 20 444 cm^{-1}). This latter band in the excitation spectrum of **3** confirms the $Tb^{3+} \rightarrow Eu^{3+}$ energy transfer.[70]

Fig. 5 shows the schematic energy levels diagram of the ground and excited states of the metal ions and ligands and the energy transfers involved in the phosphorescence of the ligands and the emission of the Tb^{3+} and Eu^{3+} ions. The activation process in the tta^- ligand is shown from the ground singlet state to the excited singlet state, then ISC among the excited singlet state of the tta^- to its triplet states, and those of the other ligands occurs followed by the energy transfer (ET) to the Tb^{3+} and Eu^{3+} ions, and finally the decay of the excited states of the metal ions to produce the emission.

PLQY and lifetime studies. The photoluminescence quantum yields (PLQY) for all the compounds are shown in Fig. 6a as the Eu^{3+} relative content function. The PLQYs increase with the Eu^{3+} content, reaching a maximum value for compound **6** with an 80/20 Eu^{3+}/Gd^{3+} ratio and decrease for contents larger than 80%. This decrease occurs by concen-

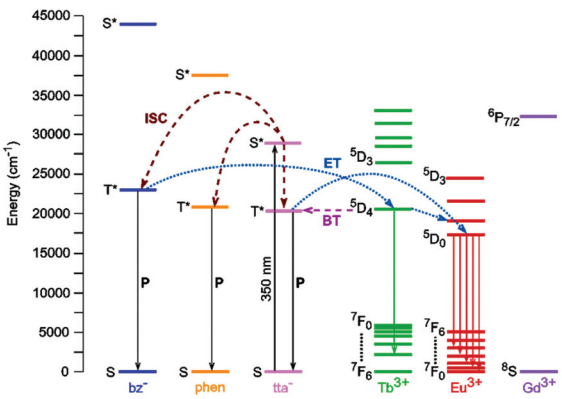

Fig. 5 Energy levels diagram and energy transfer stages in the phosphorescence and emission process. ISC, intersystem crossing; ET, energy transfer; P, phosphorescence; BT, back transfer.

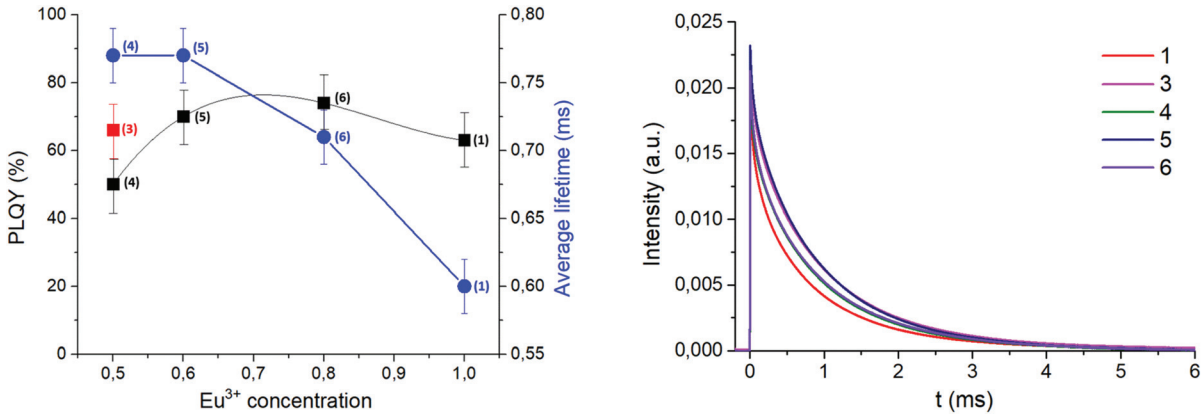

Fig. 6 (a) Average lifetimes (blue points) and Intensity of luminescence at 612 nm (black points) of **1** (0% Gd^{3+}), **4** (50% Gd^{3+}), **5** (40% Gd^{3+}), and **6** (20% Gd^{3+}) obtained for the $^5D_0$ emitting level. Red point represents the intensity of luminescence at 612 nm of **3** (50% Eu^{3+} and 50% Tb^{3+}). (b) Decay plots for **1**, **3–6** complexes.

Table 4 Average lifetimes ($\langle\tau\rangle$) of the $^5D_0$ level and photoluminescence quantum yields (PLQY) of **1**, **3–6** excited at 350 nm compared with related complexes

Compound	$\langle\tau\rangle$/ms	PLQY/%	Ref.
$[Eu_2(bz)_4(tta)_2(phen)_2]$ (**1**)	0.60	63	This work
$[EuTb(bz)_4(tta)_2(phen)_2]$ (**3**)	0.75	66	This work
	0.0008[a]		
$[EuGd(bz)_4(tta)_2(phen)_2]$ (**4**)	0.65	50	This work
$[Eu_{1.2}Gd_{0.8}(bz)_4(tta)_2(phen)_2]$ (**5**)	0.72	70	This work
$[Eu_{1.6}Gd_{0.4}(bz)_4(tta)_2(phen)_2]$ (**6**)	0.74	74	This work
$[Eu(tta)_3(phen)]$	0.98	69	45
$[Eu_2(bz)_6(phen)_2]$	1.02	48	57
$[Eu(tta)_3(DBSO)_2]$	0.71	85	68 and 71

[a] Average lifetime of the $^5D_4$ level for Tb^{3+} in **3**.

tration quenching effect in the emission, verified with the shortening of the $^5D_0$ state lifetime values as a function of the Eu^{3+} concentration (Fig. 6). The PLQY are also shown in Table 4 compared with related complexes.

The values are in the range of 50–74% for **1**, **3–6** complexes. All the compounds exhibit higher PLQY than $[Eu_2(bz)_6(phen)_2]$ (48%), which means that the inclusion of tta^- results in an improvement of the efficiency in the PL process.[57] Compared with $[Eu(tta)_3(phen)]$(69%), we find somewhat lower, but comparable, values for **3** and **4** that have lower Eu^{3+} content. However, the high Eu^{3+} content in **1** results in a low PLQY by concentration quenching. The highest values are found for **5** and **6**, which combine the occurrence of the Gd^{3+} ion and high Eu^{3+} content. In these compounds, the presence of the Gd^{3+} ion has a double effect: on the one hand, it decreases the concentration of Eu^{3+}, which results in a decrease in quenching by concentration and on the other hand, the paramagnetic character of Gd^{3+} favours the ISC in the ligands with respect to the compounds containing only the Eu^{3+} ion.[1] The sum of these two effects contributed by the bimetallic character of the compounds results in an improvement of the PLQY.

In the case of compound **3**, the paramagnetic character of Tb^{3+} leads to higher PLQY values to those of **4** with the same relative Eu^{3+} content.

The decay curves of the Eu^{3+} ($^5D_0 \rightarrow {}^7F_2$) transitions are shown in Fig. 6b and Fig. S9.† The curves are nearly exponential, and for all the samples, we calculated the average lifetimes $\langle\tau\rangle$ of the $^5D_0$ (Eu^{3+}) level with eqn (4), where $I(t)$ is the emission intensity at a time t after pulse excitation at $t = 0$.[71]

$$\langle\tau\rangle = \frac{\int_0^\infty I(t)\mathrm{d}t}{I(0)} \quad (4)$$

The average lifetimes are shown in Table 3 and plotted in Fig. 6a as a function of the Eu^{3+} content. They take values around 0.77 ms for the samples with low Eu^{3+} content and decrease to 0.6 ms for the samples with high Eu^{3+} content. The values are in agreement with those previously reported for similar complexes.[18,33] The unusual low value observed in the lifetime of the $^5D_4$ level of Tb^{3+} in **3** agrees with a fast deactivation *via* ET to the Eu^{3+} and/or back transfer to the tta^- ligand.[34,70]

EQE and *I–V* plots of the PV mini-module covered with the luminescent down-shifting films

The external quantum efficiency (EQE) corresponds to the number of charge carriers collected generated by the solar cell (SC) per incident photon on the device. The measurement of the EQE as a wavelength function shows the SC response and gives the SC characteristics. Studying the so-called intensity–voltage (*I–V*) curves allows establishing a relationship between the characteristics of the solar cell and its ability to transform solar radiation into electrical energy. The EQE as a function of the wavelength is shown in Fig. 7 for the bare mini-module (m-m), the mini-module encapsulated with pure ethylene–vinyl–acetate (EVA) and covered with a glass (m-m + EVA + glass), and the mini-module encapsulated with the luminescent down-shifting layer (LDSL) containing compounds **1**, **3–6**

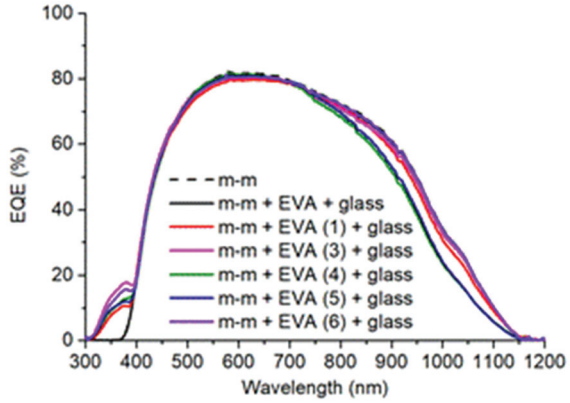

Fig. 7 EQE plot in the 300–1200 nm spectral range for the bare and encapsulated mini-module. Bare multicrystalline Si photovoltaic mini-modules, m-m; mini-modules with pure EVA covered with the glass, m-m + EVA + glass; mini-modules coated with an EVA LDSL containing compounds **1**, **3–6** covered with the glass, m-m + EVA(**1**, **3–6**) + glass.

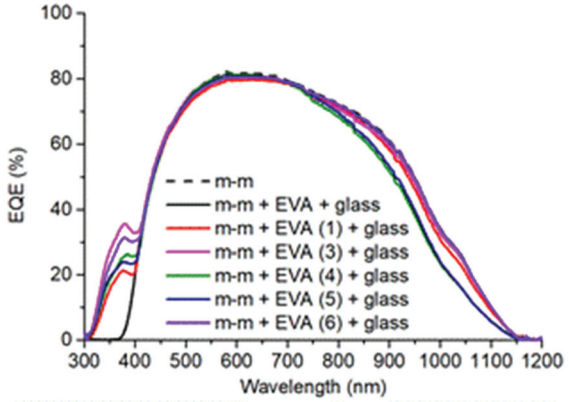

Fig. 8 EQE plot in the 300–1200 nm spectral range of the mini-module with the different LDS layers covered with an aluminium hemispherical reflector.

dispersed in EVA and covered with a glass, m-m + EVA(**1**, **3–6**) + glass.

The bare and pure EVA encapsulated mini-module is effective in the 375–1150 nm range with a maximum of EQE at 625 nm; this behaviour is typical for multi-crystalline silicon photovoltaic devices. Once the device is covered with films containing **1**, **3–6** complexes, an appreciable increase in EQE (ΔEQE) is found in the 300–400 nm spectral range, reaching maximum values in the 9.7% to 16.3% range (Table 5). This increase results from the down-shifting of the ultraviolet radiation in the LDS layer produced by the **1**, **3–6** complexes, and it is restricted to this spectral range since the DS process occurs just in this range, as we found in the PL study and absorbance plot, Fig. 3–6.[3,72]

The higher increase in the EQE is found for the heterobimetallic compounds **3** and **6**, 16.3% and 29.6%, respectively, which were found to exhibit high quantum yields in the photoluminescence study. It is also worth noting that EVA(**1**) shows the lowest activity, which could be explained by the greater effect of quenching by concentration in **1**. EVA(**4**) and EVA(**5**) show a decrease in activity above 700 nm. This behaviour is attributed to experimental limitations of the assembly of the film on the mini-module (the large number of micro shunts, the irradiation of the mini-modules in a limited area and the position of the effective area of the cell) than to a loss of efficiency in the device due to the encapsulation.[73,74] In any case, this decrease has a negative impact in the measured energy conversion, as we discuss later.

Fig. 8 shows the EQE as a function of the wavelength for the same device represented in Fig. 7, but with the device covered with an aluminium reflector that redirects most reflected and re-emitted photons to the SC (Scheme 2). Under these conditions, the EQE values result multiplied by a factor of 2, reaching values in the 20.0% to 33.8% range, indicating that half of the DS photons are not harvested in standard conditions (Table 5). This agrees with the isotropic nature of the emission that projects half of the DS photons out of the SC.[75]

To quantify the effect of the LDS layers, we calculated the increase in photo-generated current, ΔJ_{SC}, as a function of the wavelength, λ, through eqn (5).[76]

$$\Delta J_{SC} = q\int \phi(\lambda)\cdot \Delta EQE(\lambda)d\lambda = \int E_0 \cdot \Delta SR(\lambda)d\lambda \qquad (5)$$

where q is the charge of the electron, ϕ is the incident photon flux, SR is the spectral response, and E_0 is a standard reference of solar spectral irradiance according to ASTM G173-03.[77] Eqn (5) was applied to calculate the current density J_{sc} of the solar cell covered with the LDS layers in the range of 300–400 nm and the values are shown in Table 5. One can see that all the

Table 5 ΔJ_{SC} in the 300–400 nm range and ΔEQE of mc-Si PV mini-module (m-m) and the different LDS encapsulated layers calculated with eqn (2)

Device	ΔJ_{SC} (mA cm^{-2})	ΔJ_{SC} [a] (mA cm^{-2})	ΔEQE_{max} [b] (%)	ΔEQE_{max} [a,b] (%)
m-m + EVA(3) + glass	0.15	0.38	16.3	33.8
m-m + EVA(6) + glass	0.12	0.31	14.3	29.6
m-m + EVA(1) + glass	0.07	0.18	9.7	20.0
m-m + EVA(4) + glass	0.09	0.23	11.4	24.0
m-m + EVA(5) + glass	0.09	0.22	10.9	22.7

[a] With reflector. [b] At 370 nm.

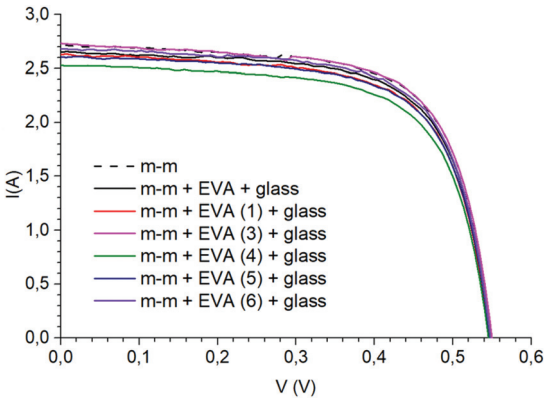

Fig. 9 *I–V* curves for the bare and encapsulated mini-module.

encapsulated LDS layers produce a measurable increase in EQE and J_{SC} with higher values for **3** and **6**.

To further investigate the impact of LDS layers on the performance of the mini-modules, we measured the *I–V* curves under standard conditions (irradiance of 1000 W m^{-2}, 25 °C, and AM 1.5), and they are shown in Fig. 9. The plots follow the typical profile with short-circuit current intensity (I_{SC}) in the 2.50–2.75 A range and open-circuit voltage (V_{OC}) of almost 0.58 V.

The characteristic parameters of the solar cell, such as the short circuit current density (J_{sc}) and the efficiency (η) through the maximum power generated by the solar cell, are shown in Table 6. With the values obtained for the mini-module encapsulated with pure EVA (m-m + EVA + glass), we calculated the gain in J_{SC} (ΔJ_{SC}) and efficiency ($\Delta\eta$) for the LDSL EVA(**1**, **3–6**) which are also shown in Table 6.

We observe a slight decrease in the J_{sc} and η for the encapsulated m-m + EVA + glass with respect to the bare m-m, which results from the absorbance and reflection of the EVA and the covering glass. Nevertheless, we obtain an increase in efficiency, $\Delta\eta$, of 0.52% and 0.21% with LDS layers containing **3** and **6** in the spectral range of the solar simulator (300–1200 nm). On the other hand, the LDS layers with **1**, **4**, and **5** show a certain decrease in those parameters because of the decrease in EQE observed above 700 nm for these LDS layers.

Conclusions

We have prepared six new bimetallic mixed-ligand coordination compounds and studied their structure, PL properties and PV applications. The combination of different ligands in the coordination sphere of the Ln^{3+} ions extends the wavelength range absorption, enhancing the excitation of the complexes and resulting in high emission quantum yields. We have observed that bridging ligands such as benzoate may lead to hetero-dinuclear complexes. The magnetic study shows an intermetallic interaction through the carboxylate bridges and confirms the composition of the bimetallic compounds. The benzoate ligand inclusion increases the energy of the lower-energy triplet state by ISC from the singlet tta^- state to the benzoate triplet, enabling the population of Tb^{3+} excited states that would not be possible without this ligand. Also, the photoluminescence study shows that the bi-metallic **3**, **5** and **6** compounds containing the paramagnetic Tb^{3+} and Gd^{3+} ions exhibit higher PLQY than the homometallic $[Eu_2(bz)_4(tta)_2(phen)_2]$; which indicates that the hetero-bimetallic character improves the complexes PL response.

Combining the bridging benzoate with phen and tta^- ligands results in molecular species dispersible in EVA polymeric films. The films can be encapsulated on a photovoltaic multi-crystalline silicon mini-module, showing UV radiation absorption and an increase in the efficiency by the down-shifting process for all the compounds in the range 300–400 nm and for compounds **3** and **6** in the spectral range 300–1200 nm.

Conflicts of interest

There are no conflicts to declare.

Acknowledgements

This publication is part of the project I+D+I RTI2018-095563-B-I00 funded by MCIN/AEI/10.13039/501100011033/FEDER "Una manera de hacer Europa". Photoluminescence study and measurements were financed by projects I+D+I PID2019-106383GB-C44 and PID2019-107335RA-I00 funded by MCIN/

Table 6 *I–V* characteristics: J_{sc} and η of the mc-Si PV mini-module (m-m) as a function of the encapsulant LDS layers. The gain in J_{SC} (ΔJ_{SC}) and efficiency ($\Delta\eta$) for the LDS layers with (**1**, **3–6**) in EVA are also shown, taking m-m + EVA + glass as the reference value

Device	J_{sc} (mA cm^{-2})	ΔJ_{sc} (mA cm^{-2})	η (%)	$\Delta\eta$ (%)
m-m	27.14(6)[a]		12.14(4)	
m-m + EVA + glass	25.80(4)		11.26(3)	
m-m + EVA(3) + glass	26.69(4)	0.92(4)	11.76(4)	0.52(4)
m-m + EVA(6) + glass	26.04(4)	0.28(4)	11.44(2)	0.21(2)
m-m + EVA(5) + glass	25.40(6)	−0.37(6)	11.18(1)	−0.06(1)
m-m + EVA(1) + glass	25.53(6)	−0.24(6)	11.18(3)	−0.08(3)
m-m + EVA(4) + glass	24.79(4)	−0.98(4)	10.72(2)	−0.52(2)

[a] Values in parenthesis are standard deviation in the last digit.

AEI/10.13039/501100011033/FEDER "Una manera de hacer Europa". GBS thanks predoctoral scholarship PRE2019-087522 funded by MCIN/AEI/10.13039/501100011033 y FSE "El FSE invierte en tu futuro".

References

1 K. Binnemans, *Chem. Rev.*, 2009, **109**, 4283–4374.
2 T. Monzón-Hierro, J. Sanchiz, S. González-Pérez, B. González-Díaz, S. Holinski, D. Borchert, C. Hernández-Rodríguez and R. Guerrero-Lemus, *Sol. Energy Mater. Sol. Cells*, 2015, **136**, 187–192.
3 R. Guerrero-Lemus, J. Sanchiz, M. Sierra, I. R. Martín, C. Hernández-Rodríguez and D. Borchert, *Sol. Energy Mater. Sol. Cells*, 2018, **185**, 312–317.
4 T. Fix, A. Nonat, D. Imbert, S. Di Pietro, M. Mazzanti, A. Slaoui and L. J. Charbonnière, *Prog. Photovoltaics: Res. Appl.*, 2016, **24**, 1251–1260.
5 F. M. Cabral, D. A. Gálico, I. O. Mazali and F. A. Sigoli, *Inorg. Chem. Commun.*, 2018, **98**, 29–33.
6 T. Gorai, W. Schmitt and T. Gunnlaugsson, *Dalton Trans.*, 2021, **50**, 770–784.
7 R. Gao, M. S. Kodaimati and D. Yan, *Chem. Soc. Rev.*, 2021, **50**, 5564–5589.
8 S. Wang, J. Jiang, Y. Lu, J. Liu, X. Han, D. Zhao and C. Li, *J. Lumin.*, 2020, **226**, 117418.
9 T. Y. Popelensky and V. V. Utochnikova, *Dalton Trans.*, 2020, **49**, 12156–12160.
10 D. Yang, H. Liang, Y. Liu, M. Hou, L. Kan, Y. Yang and Z. Zang, *Dalton Trans.*, 2020, **49**, 4725–4731.
11 C. M. B. Leite Silva, A. G. Bispo-Jr, S. A. M. Lima and A. M. Pires, *Opt. Mater.*, 2019, **96**, 109323.
12 S. F. H. Correia, A. R. N. Bastos, L. Fu, L. D. Carlos, P. S. André and R. A. S. Ferreira, *Opto-Electron. adv.*, 2019, **2**, 19000601–19000608.
13 A. Gavriluta, T. Fix, A. Nonat, A. Slaoui, J.-F. Guillemoles and L. J. Charbonnière, *Eur. J. Inorg. Chem.*, 2017, 5318–5326.
14 M. Li, Y. Zhou, Y. Yao, T. Gao, P. Yan and H. Li, *Dalton Trans.*, 2021, **50**, 9914–9922.
15 A. Topor, D. Avram, R. Dascalu, C. Maxim, C. Tiseanu and M. Andruh, *Dalton Trans.*, 2021, **50**, 9881–9890.
16 Y. Kitagawa, F. Suzue, T. Nakanishi, K. Fushimi and Y. Hasegawa, *Dalton Trans.*, 2018, **47**, 7327–7332.
17 A. I. S. Silva, N. B. D. Lima, A. M. Simas and S. M. C. Goncalves, *ACS Omega*, 2017, **2**, 6786–6794.
18 K. Binnemans, *Coord. Chem. Rev.*, 2015, **295**, 1–45.
19 Y. Ma and Y. Wang, *Coord. Chem. Rev.*, 2010, **254**, 972–990.
20 Y. Hasegawa, Y. Kitagawa and T. Nakanishi, *NPG Asia Mater.*, 2018, **10**, 52–70.
21 E. Klampaftis, D. Ross, K. R. McIntosh and B. S. Richards, *Sol. Energy Mater. Sol. Cells*, 2009, **93**, 1182–1194.
22 B. González-Díaz, M. H. Saw, C. Hernández-Rodríguez, J. Sanchiz, Y. S. Khoo and R. Guerrero-Lemus, *Mater. Sci. Eng., B*, 2020, **261**, 114763.
23 L. V. Meyer, F. Schonfeld and K. Muller-Buschbaum, *Chem. Commun.*, 2014, **50**, 8093–8108.
24 M. Latva, H. Takalo, V.-M. Mukkala, C. Matachescu, J. C. Rodríguez-Ubis and J. Kankare, *J. Lumin.*, 1997, **75**, 149–169.
25 X. P. Yang, B. S. Kang, W. K. Wong, C. Y. Su and H. Q. Liu, *Inorg. Chem.*, 2003, **42**, 169–179.
26 L. Abad Galan, B. L. Reid, S. Stagni, A. N. Sobolev, B. W. Skelton, E. G. Moore, G. S. Hanan, E. Zysman-Colman, M. I. Ogden and M. Massi, *Dalton Trans.*, 2018, **47**, 7956–7964.
27 V. I. Tsaryuk and K. P. Zhuravlev, *J. Lumin.*, 2021, **237**, 118159.
28 L. R. Melby, N. J. Rose, E. Abramson and J. C. Caris, *J. Am. Chem. Soc.*, 1964, **86**, 5117–5125.
29 W. Li, P. Yan, G. Hou, H. Li and G. Li, *Dalton Trans.*, 2013, **42**, 11537–11547.
30 O. Moudam, B. C. Rowan, M. Alamiry, P. Richardson, B. S. Richards, A. C. Jones and N. Robertson, *Chem. Commun.*, 2009, 6649–6651.
31 Z. Abbas, P. Singh, S. Dasari, S. Sivakumar and A. K. Patra, *New J. Chem.*, 2020, **44**, 15685–15697.
32 J. Shi, Y. Hou, W. Chu, X. Shi, H. Gu, B. Wang and Z. Sun, *Inorg. Chem.*, 2013, **52**, 5013–5022.
33 H. F. Li, P. F. Yan, P. Chen, Y. Wang, H. Xu and G. M. Li, *Dalton Trans.*, 2012, **41**, 900–907.
34 V. V. Khistiaeva, A. S. Melnikov, S. O. Slavova, V. V. Sizov, G. L. Starova, I. O. Koshevoy and E. V. Grachova, *Inorg. Chem. Front.*, 2018, **5**, 3015–3027.
35 M. Fairley, M. M. V. S. Livera, W. Chen, J. H. S. K. Monteiro, A. Schmitt, A. de Bettencourt-Dias, S. Roberts and Z. Zheng, *J. Rare Earths*, 2021, **39**, 487–494.
36 P. A. Demakov, A. A. Ryadun, P. V. Dorovatovskii, V. A. Lazarenko, D. G. Samsonenko, K. A. Brylev, V. P. Fedin and D. N. Dybtsev, *Dalton Trans.*, 2021, **50**, 11899–11908.
37 S. Xing and C. Janiak, *Chem. Commun.*, 2020, **56**, 12290–12306.
38 F. Saraci, V. Quezada-Novoa, P. R. Donnarumma and A. J. Howarth, *Chem. Soc. Rev.*, 2020, **49**, 7949–7977.
39 W. Gao, H. Wei, C. L. Wang, J. P. Liu and X. M. Zhang, *Dalton Trans.*, 2021, **50**, 11619–11630.
40 K. M. Kuznetsov, M. I. Kozlov, A. N. Aslandukov, A. A. Vashchenko, A. V. Medved'ko, E. V. Latipov, A. S. Goloveshkin, D. M. Tsymbarenko and V. V. Utochnikova, *Dalton Trans.*, 2021, **50**, 9685–9689.
41 Angilent Technologies, *XCalibur CCD System, CRISALISPRO Software System, Version 1.171.36.24*, 2012.
42 G. M. Sheldrick, *Acta Crystallogr., Sect. C: Struct. Chem.*, 2015, **71**, 3–8.
43 C. B. Hubschle, G. M. Sheldrick and B. Dittrich, *J. Appl. Crystallogr.*, 2011, **44**, 1281–1284.
44 K. Brandenburg and H. Putz, *Diamond (Version 3.2), Crystal and Molecular Structure Visualization*, 2009.
45 F. R. G. Silva, J. F. S. Menezes, G. B. Rocha, S. Alves, H. F. Brito, R. L. Longo and O. L. Malta, *J. Alloys Compd.*, 2000, **303–304**, 364–370.

46 U. Blieske and G. Stollwerck, in *Semicond. Semimet*, ed. G. P. Willeke and E. R. Weber, Elsevier, 2013, vol. 89, pp. 199–258.
47 S. K. Gaddam, R. Pothu and R. Boddula, *J. Materiomics*, 2021, **7**, 920–928.
48 R. Satpathy and V. Pamuru, *Chapter 5 - Manufacturing of crystalline silicon solar PV modules*, Academic Press, 2021.
49 M. Spiegel, *Sol. Energy Mater. Sol. Cells*, 1998, **55**, 331–340.
50 C. H. Seaman, *Sol. Energy*, 1982, **29**, 291–298.
51 R. Guerrero-Lemus, J. Sanchiz, M. Sierra-Ramos, I. R. Martín, C. Hernández-Rodríguez and D. Borchert, *Sens. Actuators, A*, 2018, **271**, 60–65.
52 S. González-Pérez, J. Sanchiz, V. D. Rodríguez, D. Cañadillas-Ramallo, J. González-Platas, D. Borchert, B. González-Díaz, C. Hernández-Rodríguez and R. Guerrero-Lemus, *J. Lumin.*, 2018, **201**, 148–155.
53 B. González-Díaz, M. Sierra-Ramos, J. Sanchiz and R. Guerrero-Lemus, *Sens. Actuators, A*, 2018, **276**, 312–319.
54 S. González-Pérez, J. Sanchiz, B. González-Díaz, S. Holinski, D. Borchert, C. Hernández-Rodríguez and R. Guerrero-Lemus, *Surf. Coat. Technol.*, 2015, **271**, 106–111.
55 J. Cepeda, S. Perez-Yanez, G. Beobide, O. Castillo, J. A. Garcia, M. Lanchas and A. Luque, *Dalton Trans.*, 2015, **44**, 6972–6986.
56 A. W.-H. Lam, W.-T. Wong, S. Gao, G. Wen and X.-X. Zhang, *Eur. J. Inorg. Chem.*, 2003, 149–163.
57 O. T. Alexander, R. E. Kroon, A. Brink and H. G. Visser, *Dalton Trans.*, 2019, **48**, 16074–16082.
58 H. Bußkamp, G. B. Deacon, M. Hilder, P. C. Junk, U. H. Kynast, W. W. Lee and D. R. Turner, *CrystEngComm*, 2007, **9**, 394–411.
59 L. Canadillas-Delgado, O. Fabelo, J. Pasan, F. S. Delgado, F. Lloret, M. Julve and C. Ruiz-Perez, *Dalton Trans.*, 2010, **39**, 7286–7293.
60 R. Boča, *Coord. Chem. Rev.*, 2004, **248**, 757–815.
61 J. W. de Oliveira Maciel, M. A. Lemes, A. K. Valdo, R. Rabelo, F. T. Martins, L. J. Queiroz Maia, R. C. de Santana, F. Lloret, M. Julve and D. Cangussu, *Inorg. Chem.*, 2021, **60**, 6176–6190.
62 O. Kahn, *Molecular Magnetism*, VCH, New York, 1993.
63 R. Baggio, R. Calvo, M. T. Garland, O. Pena, M. Perec and A. Rizzi, *Inorg. Chem.*, 2005, **44**, 8979–8987.
64 O. Roubeau, G. Lorusso, S. J. Teat and M. Evangelisti, *Dalton Trans.*, 2014, **43**, 11502–11509.
65 S. C. Manna, E. Zangrando, J. Ribas and N. Ray Chaudhuri, *Polyhedron*, 2006, **25**, 1779–1786.
66 A. Rohde and W. Urland, *Dalton Trans.*, 2006, 2974–2978.
67 I. Georgieva, N. Trendafilova, T. Zahariev, N. Danchova and S. Gutzov, *J. Lumin.*, 2018, **202**, 192–205.
68 O. L. Malta, H. F. Brito, J. F. S. Menezes, f. R. G. E. Silva, S. Alves, F. S. Farias and A. V. M. de Andrade, *J. Lumin.*, 1997, **75**, 255–268.
69 W. R. Dawson, J. L. Kropp and M. W. Windsor, *J. Chem. Phys.*, 1966, **45**, 2410–2418.
70 A. N. Carneiro Neto, R. T. Moura, A. Shyichuk, V. Paterlini, F. Piccinelli, M. Bettinelli and O. L. Malta, *J. Phys. Chem. C*, 2020, **124**, 10105–10116.
71 S. González-Pérez, I. R. Martín, F. Lahoz, P. Haro-González and J. Herreros, *Appl. Phys. A*, 2008, **93**, 983–986.
72 R. Rothemund, *Sol. Energy Mater. Sol. Cells*, 2014, **120**, 616–621.
73 R. Scheer and H.-W. Schock, *Chalcogenide Photovoltaics: Physics, Technologies, and Thin Film Devices*, Wiley-VCH Verlag GmbH & Co. KGaA, 2011.
74 F. Fertig, M. Padilla, O. Breitenstein, H. Höffler, I. Geisemeyer, M. C. Schubert and S. Rein, *Energy Procedia*, 2015, **77**, 43–56.
75 L. Li, *Opt. Lasers Eng.*, 2000, **34**, 231–253.
76 J. Liu, K. Wang, W. Zheng, W. Huang, C.-H. Li and X.-Z. You, *Prog. Photovoltaics: Res. Appl.*, 2013, **21**, 668–675.
77 ASTM G173-03(2020), *Standard Tables for Reference Solar Spectral Irradiances: Direct Normal and Hemispherical on 37° Tilted Surface*, ASTM International, West Conshohocken, PA, 2020, http://www.astm.org, DOI: 10.1520/G0173-03R20.

